Acta Crystallographica Section A
Foundations of Crystallography
ISSN 0108-7673

Received 10 September 2009
Accepted 13 November 2009

Photoinduced structural dynamics of polar solids studied by femtosecond X-ray diffraction

Thomas Elsaesser* and Michael Woerner

Max-Born-Institut für Nichtlineare Optik und Kurzzeitspektroskopie, D-12489 Berlin, Germany.
Correspondence e-mail: elsasser@mbi-berlin.de

Femtosecond X-ray diffraction allows for real-time mapping of structural changes in condensed matter on atomic length and timescales. Sequences of diffraction patterns provide both transient geometries and charge-density maps of crystalline materials. This article reviews recent progress in this field, the main emphasis being on experimental work done with laser-driven hard X-ray sources. Both Bragg diffraction techniques for bulk and nanostructured single crystals as well as the recently implemented powder diffraction from polycrystalline samples are discussed. In ferroelectric superlattice structures, coherent phonon motions and the driving stress mechanisms are observed in real time. In molecular crystals charge-transfer processes and the concomitant changes of the lattice geometry are analyzed.

1. Introduction

X-ray diffraction represents a major technique for determining the atomic structure of matter. In the condensed phase, equilibrium structures of an impressive range of inorganic and organic crystalline materials have been studied. Using hard X-rays with photon energies in the 10 keV range, interatomic distances or bond lengths have been derived from diffraction patterns with a precision of up to approximately 1 pm (Warren, 1969; Als-Nielsen & McMorrow, 2001). Both Bragg diffraction of monochromatic X-rays and Laue diffraction of X-rays in a broad spectral range have been applied. X-rays interact with the electrons in the crystal, most of which are bound to the atoms and the intensity of the diffraction peaks is determined by Fourier transform of the three-dimensional electron density. This fact allows for deriving charge-density maps, *i.e.* the distribution of electronic charge in the crystal (Coppens, 1997).

In many systems, processes governing physical, chemical or biological function are connected with structure changes on a multitude of timescales. In crystal lattices, the intrinsic time range of atomic motion is below 1 ps, as determined by the multidimensional potential energy surfaces for translational, rotational or vibrational motions. Mapping such ultrafast structural dynamics in real time requires X-ray diffraction pattern sequences to be recorded with a femtosecond time resolution (Rousse, Rischel & Gauthier, 2001; Rischel *et al.*, 1997; Siders *et al.*, 1999; Rousse, Rischel, Fourmaux *et al.*, 2001; Bargheer *et al.*, 2006). This is possible by applying a pump–probe approach in which excitation by an ultrashort optical pulse initiates the structural change and a femtosecond hard X-ray pulse is diffracted from the excited sample. The measurement of diffraction patterns for different delay times of the X-ray pulse relative to the excitation pulse provides a sequence of 'snapshots' from which the momentary atomic positions and/or charge distributions can be derived. With respect to structural information this approach is much more direct than ultrafast optical spectroscopies, providing the transient dielectric function of the system under study.

The potential of femtosecond X-ray diffraction for unraveling microscopic structural dynamics has initiated a worldwide effort to implement this technique for applications in physics, chemistry and biology. A key issue is the generation of femtosecond hard X-ray pulses which are synchronized with an optical excitation pulse (Service, 2002). A variety of generation schemes have been demonstrated and applied, such as laser-driven plasma sources (Kmetec *et al.*, 1991; Siders *et al.*, 1999; Korn *et al.*, 2002; Jiang *et al.*, 2002), slicing schemes in which femtosecond pulses are derived from the 50 to 100 ps long pulses of a synchrotron (Schoenlein *et al.*, 2000; Khan *et al.*, 2006; Beaud *et al.*, 2007), and electron accelerators in combination with undulator insertion devices (Lindenberg *et al.*, 2005), a basic technology for free electron lasers.

In this article we review recent progress in mapping ultrafast structural dynamics by X-ray diffraction with a femtosecond time resolution. We focus on experiments performed with laser-driven plasma sources for ultrashort hard X-ray pulses to elucidate the dynamic properties of polar crystals characterized by different degrees of static and/or transient charge separation in their lattice. Results are presented for two classes of materials:

(i) perovskite superlattice structures consisting of a sequence of metallic and ferroelectric nanolayers, and

(ii) organic and inorganic molecular materials in single-crystal or polycrystalline form.

We show how to derive quantitative information on the microscopic lattice dynamics and the mechanisms driving them from the time-resolved diffraction data. The article is

organized as follows. In §2 we discuss the generation of femtosecond hard X-ray pulses and the diffraction methods applied. Results on superlattice structures and molecular materials are presented in §§3 and 4, respectively. Conclusions and a perspective of future developments are given in the final section (§5).

2. Laser-driven femtosecond X-ray sources and diffraction techniques

2.1. Ultrashort hard X-ray pulses from laser-driven plasma sources

The irradiation of metal targets by femtosecond laser pulses with a peak intensity higher than 10^{16} W cm^{-2} results in the generation of plasma that emits radiation in the hard X-ray range (Kmetec *et al.*, 1991; Siders *et al.*, 1999; Korn *et al.*, 2002; Jiang *et al.*, 2002). The key mechanism is the acceleration of free electrons into the target by the very high electric field of the pulses and the generation of characteristic radiation and *Bremsstrahlung* by interactions with target atoms. The characteristic emission originates from the transition of an outer-shell electron into the inner-shell (core) hole of target atoms with a lifetime of the outer-shell state of a few femtoseconds, much shorter than the driving laser pulses. The time structure of the characteristic emission is determined by the period over which the acceleration field is applied, *i.e.* the laser pulse duration, and the propagation time of the electrons in the target. For a target thickness of the order of 10–20 µm, the characteristic emission has a duration of the order of 100 fs.

While the first generation of femtosecond X-ray plasma sources has worked at low repetition rates of 1–20 Hz, recent developments in laser and target technologies have allowed for generating hard X-ray pulses with a kilohertz repetition rate and much smaller intensity fluctuations (Korn *et al.*, 2002; Jiang *et al.*, 2002; Zhavoronkov *et al.*, 2005; Zamponi *et al.*, 2009). At a 1 kHz repetition rate, amplified Ti:sapphire lasers routinely provide sub-50 fs pulses with energies of 5–10 mJ, corresponding to average optical powers of 5–10 W. Such pulses can be focused to sub-10 µm diameters on the target, thus reaching the required peak intensities higher than 10^{16} W cm^{-2}. At such intensities, the irradiated target area is damaged irreversibly and, consequently, moving targets providing a fresh area for each laser pulse are required. In addition, a highly stable spatial position of the target area with fluctuations of less than 10–20 µm is needed. Such requirements are fulfilled by modern target technologies making use of either liquid metal jets or metal wires or tapes moving with sufficient speed.

A scheme of the prototype sources developed in our laboratory is shown in Fig. 1(*a*) (Zhavoronkov *et al.*, 2005; Zamponi *et al.*, 2009). An amplified Ti:sapphire laser system provides sub-50 fs pulses at 800 nm with an energy of up to 5 mJ per pulse and a repetition rate of 1 kHz. Part of the laser output (10%) serves as a pump pulse to excite the sample, either at the fundamental laser wavelength of 800 nm or after nonlinear optical frequency conversion (NLO). The major fraction of the laser output (90%) drives the X-ray plasma source contained in a vacuum chamber. A parabolic mirror outside the vacuum chamber focuses the laser pulses onto a 20 µm thick copper tape (spot diameter ≤ 5 µm) to generate Cu $K\alpha$ radiation in a forward direction. The Cu tape moves at a speed of 4 cm s^{-1} to expose a fresh surface for each laser pulse. A moving plastic tape (thickness 175 µm) protects the entrance window of the vacuum chamber against debris and a second plastic tape of 35 µm thickness seals the output slit through which the X-ray pulses leave the chamber. For radiation safety, the source chamber is mounted in a movable lead housing.

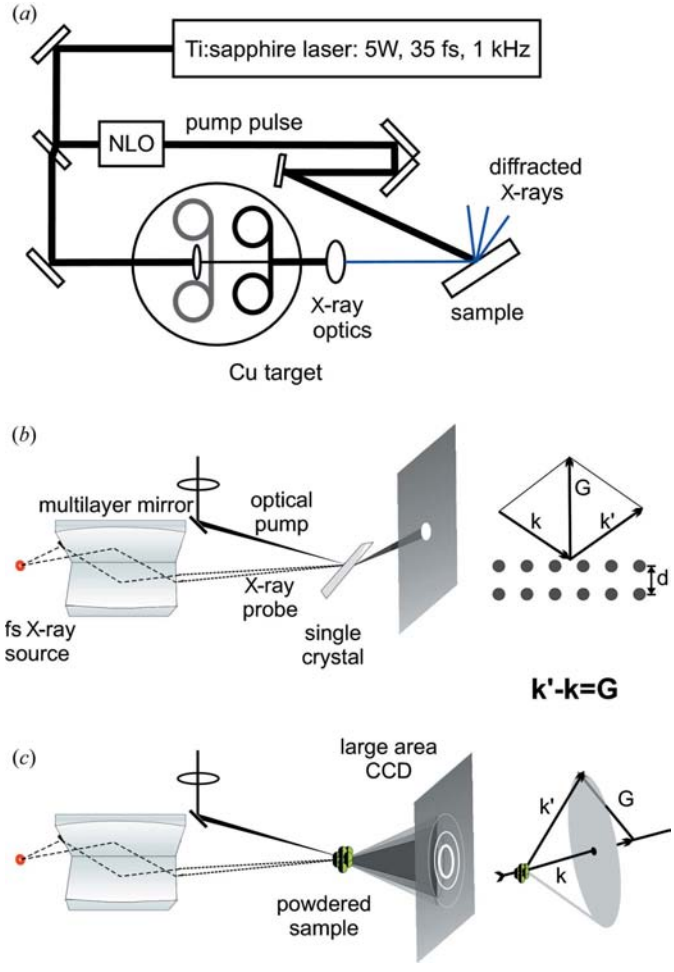

Figure 1
(*a*) Setup for femtosecond optical pump/hard X-ray probe experiments. To generate X-rays in a plasma source working at a 1 kHz repetition rate, the main part of the output of an amplified Ti:sapphire laser is focused onto a 20 µm thick copper-tape target placed in a vacuum chamber. The X-rays emitted in a forward direction are focused onto the sample by multilayer X-ray optics. The diffraction signals are detected with a X-ray charge-couple device (CCD) detector. The sample is optically excited by a second part of the laser output at 800 nm or by frequency-converted (NLO) pump pulses. The diffracted X-ray signals are measured as a function of pump–probe delay. (*b*) Scheme of a Bragg diffraction experiment on single-crystal samples. The Bragg condition is illustrated schematically on the right-hand side. (*c*) Scheme of a powder diffraction experiment with polycrystalline samples. A multitude of diffracted Debye–Scherrer rings (*cf.* illustration of **k**-vector geometry on the right-hand side) is detected with a large-area X-ray CCD detector.

Table 1
Properties of the femtosecond X-ray plasma source.

Laser pulse energy (mJ)	5
Repetition rate (kHz)	1
Laser pulse duration (fs)	35
Laser intensity (W cm^{-2})	$\leq 10^{18}$
Cu $K\alpha$ photon energy (keV)	8.04
X-ray photons emitted (photons s^{-1})	5×10^{10}
Conversion efficiency	1.5×10^{-5}
Source dimension (μm)	10 ± 2
X-ray pulse duration (fs)	100–200
X-ray photons on sample (photons s^{-1})	~10^6
X-ray spot dimension on sample (μm)	30–200

The X-ray pulses are focused onto the sample with a multilayer optics collecting a solid angle of 10^{-3} and showing reflectivities of up to 0.8 for $K\alpha$ radiation (Bargheer *et al.*, 2005). The forward geometry for generating the X-ray pulses allows for a convenient measurement of delay zero when the pump and probe interact simultaneously with the sample, by removing the metal target and recording the cross-correlation of the 800 nm driving pulse with the pump pulse (Korff Schmising *et al.*, 2007*b*). The main features of the X-ray source are summarized in Table 1; a more detailed description has been given in Zamponi *et al.* (2009). The driving laser, the X-ray source, the setup for generating pump pulses and the diffraction experiment fit onto a conventional experimental table (area approximately 5 m^2), similar to all-optical femtosecond experiments.

2.2. Mapping ultrafast structural dynamics

Most experiments addressing ultrafast structural dynamics in real time have made use of a pump–probe scheme where an optical pump pulse initiates the structure-changing processes and a hard X-ray probe pulse is diffracted from the excited sample (Rousse, Rischel & Gauthier, 2001; Bargheer *et al.*, 2006). Changes of intensity and angular position of the diffraction peaks have been measured as a function of pump–probe delay. Owing to the fixed wavelength of X-ray pulses from plasma sources, one relies on measurements of the angular position and strength of single or small groups of Bragg peaks from single crystals or – as introduced very recently by us – of Debye–Scherrer rings from polycrystalline powder samples. The respective experimental geometries and **k**-vector diagrams are shown in Figs. 1(*b*) and (*c*), where **k** and **k**′ represent the **k** vectors of the incoming and the scattered X-rays and **G** is a reciprocal-lattice vector (d = spacing of lattice planes). The diffracted X-rays are detected in a spatially resolved way with the help of an X-ray CCD detector.

Key issues of this experimental approach are time resolution and the sensitivity for measuring changes of diffracted intensity. The time resolution is determined by the durations of optical pump and X-ray probe pulses, the degree of their synchronization, the propagation geometry of pump and probe in the sample, and the X-ray scattering geometry. For laser-driven plasma sources, the timing jitter between pump and probe is negligible compared with the duration of the pulses. The group velocity mismatch between the optical and the X-ray pulses limits the effective interaction length (sample thickness) to values of less than 100 μm if a time resolution of the order of 100 fs is required. In strongly absorbing crystalline samples, the penetration depth of the pump is typically well below this limit. In powder samples, the strong elastic scattering of the optical pump pulse limits its penetration depth to a few tens of microns.

The highly stable X-ray sources working at kilohertz repetition rates allow for studying subtle structural changes, in particular fully reversible processes (Sokolowski-Tinten *et al.*, 2003; Bargheer *et al.*, 2004; Cavalleri *et al.*, 2006; Korff Schmising *et al.*, 2007*a*). In general, changes in the lattice constants and geometries can be derived from changes in the diffraction angle $\Delta\Theta/\Theta_0$ and of the diffracted intensity $\Delta I/I_0 = (I - I_0)/I_0$, where I_0 and Θ_0 are the diffracted intensity and the diffraction angle for the unexcited sample. A fundamental limit of the dynamic range over which such quantities can be measured is set by the photon-counting statistics in the X-ray detection process. The diffraction efficiency into a single Bragg peak or a single Debye–Scherrer diffraction ring has values between 10^{-3} and 10^{-5} for a wide range of materials. For an incoming X-ray flux of 10^6 photons per s on the sample, between 10 and 1000 diffracted X-ray photons per s are detected. For typical data-acquisition times of 20 min, the total number of counts is between $N_{\rm tot} = 1.2 \times 10^4$ and 1.2×10^6. The statistical error $\Delta N/N_{\rm tot} = 1/(N_{\rm tot})^{1/2}$ has values between 10^{-2} and 10^{-3}. Such numbers set a limit for the smallest $\Delta I/I_0$ that can be measured in a time-resolved experiment. In our experiments the actual noise was typically twice that expected from the photon statistics. The smallest changes in lattice constants determined so far are of the order of $\Delta a/a_0 = 10^{-5}$ (Korff Schmising *et al.*, 2006).

3. Lattice dynamics in superlattice structures

The concept of superlattice (SL) structures has been introduced to tailor the electronic bandstructure of semiconductors in a wide range and to optimize device performance (Esaki & Tsu, 1970). Later, SL structures have been studied for a wide range of other materials, including metals, ferroelectrics and magnetic materials. The current technologies of epitaxial growth and layer deposition allow for generating SLs of very high structural quality, *i.e.* atomically sharp interfaces between the monocrystalline structure of the different layers. In their simplest form, SLs consist of a sequence of nanometre-thick layer pairs made from two different materials. SLs display structural periodicities on two different length scales, the subnanometre lattice constants of the crystalline materials and the nanometre thickness of the layer pairs $d_{\rm SL}$ (Fig. 2*a*).

In the static X-ray Bragg diffraction pattern, the SL periodicity results in a series of SL diffraction peaks around the bulk Bragg peaks of the layer materials occurring at $2\pi/a_A$ and $2\pi/a_B$ (or multiples) for the two materials A and B (Krost *et al.*, 1996). The SL peaks are equally spaced occurring at

multiples of the reciprocal SL vector $g_{SL} = 2\pi/d_{SL}$. The intensity envelope of the SL Bragg pattern is determined by the envelopes of the individual SL layers, as schematically shown in the lower panel of Fig. 2(*a*). The diffraction pattern of a perovskite SL sample consisting of 15 pairs of a 4.92 nm thick $PbZr_xTi_{1-x}O_3$ (PZT) and a 6.29 nm thick $SrRuO_3$ (SRO) layer (d_{SL} = 11.21 nm) is presented in Fig. 2(*c*) (thick solid line), displaying a series of SL peaks around the (002) bulk peak from the $SrTiO_3$ (STO) substrate. The pattern is well reproduced by calculations based on dynamical diffraction theory (dash–dotted line).

The nanometre SL periodicity also affects the acoustic phonon dispersion of the layered materials. Along the SL stack axis, a so-called mini Brillouin zone of width $\pm\pi/d_{SL}$ forms into which the bulk phonon branches are folded back (Fig. 2*b*). The modified k dispersion now intersects the k = 0 axis and displays energy gaps at $k = 0$ and $\pm\pi/d_{SL}$ (Colvard *et al.*, 1985). In the SL structure, a subset of such so-called SL phonons change the thickness of the layer pairs along the stacking axis.

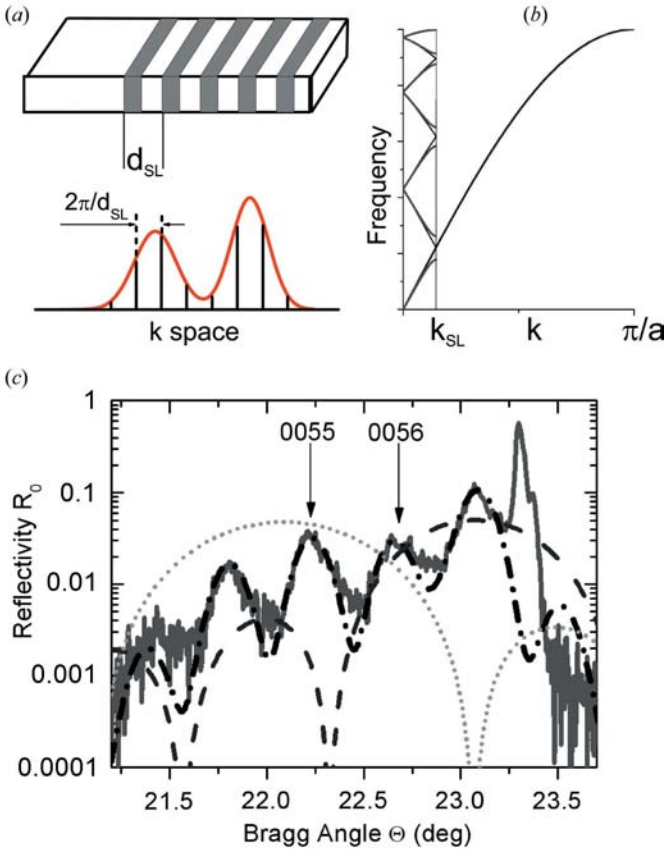

Figure 2
(*a*) Upper panel: schematic of a superlattice (SL) geometry consisting of a sequence of layer pairs with thickness d_{SL}, the SL period. Lower panel: schematic X-ray diffraction pattern from an SL displaying a series of SL Bragg peaks with a constant spacing of $g_{SL} = 2\pi/d_{SL}$. The envelopes of the Bragg pattern are determined by the structure factors of the two different types of SL layers. (*b*) Schematic of the SL phonon dispersion in a mini Brillouin zone with width $\pm k_{SL} = \pm\pi/d_{SL}$ that is much narrower than the bulk Brillouin zone with $k = \pi/a$ (a: lattice constant). (*c*) Static X-ray diffraction pattern of a PZT/SRO SL (thick line) displaying a series of SL peaks and the (002) Bragg peak of the STO substrate. Dash–dotted line: X-ray reflectivity of the sample calculated from dynamical X-ray diffraction theory. The dotted and dashed lines give the envelope functions determined by the individual PZT and SRO layers.

Ultrafast optical excitation of an SL allows for launching coherent SL phonon excitations. In particular, one can generate phonon wavepackets periodically modulating the thickness of the individual layers while leaving the total thickness d_{SL} of the layer pairs constant. In this type of SL motion, the expansion of one layer compensates for the compression of the other and *vice versa*. Such lattice dynamics are directly mapped into the X-ray diffraction pattern of the SL. For constant d_{SL}, the angular position of the SL Bragg peaks remains unchanged. Their intensity, however, is periodically modulated owing to the angular shifts of the intensity envelopes determined by the individual layers (*cf.* Fig. 2*a*). As a result, the periodic SL elongations are manifested in a periodic intensity modulation of SL peaks. Sequences of X-ray diffraction patterns measured in a femtosecond optical pump and X-ray probe scheme reveal the intensity modulations directly. Applying this concept, we have studied a variety of semiconductor, ferroelectric and ferromagnetic SLs (Bargheer *et al.*, 2004; Korff Schmising *et al.*, 2007*a*, 2008). In the following, we briefly discuss some of the results.

Ferroelectricity of a wide class of perovskite materials is due to a spatial displacement of positive and negative ionic charges in the crystal lattice (Wolfram & Ellialtioglu, 2006). In Fig. 3(*a*), we show the unit cell of PZT with positive Pb^{2+} and Ti^{4+}/Zr^{4+} ions and negative O^{2-} ions in the characteristic octahedral arrangement. The two relevant lattice coordinates are the tetragonality $\eta = c/a$ and the soft-mode coordinate $\xi_{Pb-Ti} = \xi_{Pb-O} - \xi_{Ti-O}$ (Lichtensteiger *et al.*, 2005; Sanjurjo *et al.*, 1983). The ferroelectric polarization P is proportional to ξ_{Pb-Ti} with $P/P_0 = \xi/\xi_0$, where ξ_0 and P_0 are the equilibrium values. The two lattice coordinates η and ξ are anharmonically coupled through a third-order term in the crystal Hamiltonian proportional to $\eta\xi^2_{Pb-Ti}$. Thus, a change of tetragonality modifies the ferroelectric polarization, a mechanism that allows for *static* strain engineering along the c axis to tailor the ferroelectric properties of SLs. An ultrafast change of tetragonality by launching SL phonon wavepackets should result in a periodic, *i.e. dynamic*, change in the ferroelectric properties.

In the experiments of Korff Schmising *et al.* (2007*a*), an SL consisting of 15 pairs of 4.92 nm thick PZT and 6.29 nm thick SRO layers ($d_{SL} = d_{PZT} + d_{SRO}$ = 11.21 nm) was studied. The SL was grown on an STO substrate with the c axis of the layers parallel to the stacking axis. A 50 fs pump pulse at 800 nm excited the SRO layers exclusively, thus generating an electronic excitation with a spatial period d_{SL}. Electron–phonon coupling in the excited SRO layers results in the generation of transient stress along the c axis, which drives SL motions. Such motions are mapped by measuring changes of intensity and/or angular position on a number of SL diffraction peaks, in particular the (0,0,55) and (0,0,56) peaks. The (0,0,56) peak is located at a Bragg angle where the slope of the PZT and SRO envelope functions is substantial, making the intensity of this

peak most sensitive to angular shifts of the envelopes by changes of the individual layer thicknesses. In this way, motions along the coordinate η are measured. The (0,0,55) reflection is located at the maximum of the PZT envelope function and its intensity is particularly sensitive to the ionic displacement ξ_{Pb-Ti} within the PZT unit cell.

In Fig. 3(*b*), the change in X-ray diffracted intensity measured in a reflection geometry, $\Delta R/R_0$, is plotted as a function of pump–probe delay for the (0,0,56) (circles) and (0,0,55) (diamonds) Bragg peaks (excitation fluence 5 mJ cm^{-2}). The reflectivity changes display a delayed rise, followed by oscillations of opposite sign. The angular position of both SL peaks (not shown) is constant within 4 ps after excitation and then gradually changes over a 30 ps period to reach a new value that is constant over hundreds of picoseconds. This shift reflects the thermal expansion of the entire SL connected with the propagation of acoustic phonons. From the absolute value of the angular shift, a maximum change of $\Delta d_{SL}/d_{SL} = 3 \times 10^{-3}$ for the SL period d_{SL} is estimated.

The oscillatory reflectivity changes on the (0,0,56) and (0,0,55) SL peaks are driven by the photogenerated stress along the *c* axis of the SL. Electron–phonon coupling causes a delayed rise of stress with a time constant of approximately 500 fs, which is short compared with the oscillation period of approximately 2 ps. A small fraction of the initial excitation energy in the electronic system is converted into a coherent SL excitation along the lattice coordinate η. This stress, which is of impulsive character on the timescale of the SL oscillation period, generates the oscillatory motion of the SL manifested in the intensity oscillations of the two SL diffraction peaks. The SL oscillations are equivalent to a coherent superposition of SL phonon states (*cf.* Fig. 2*b*) in a wavepacket periodically modulating the tetragonality η.

Any change in the tetragonaliy η results in a change of the soft-mode elongation ξ because of the anharmonic coupling of the two lattice modes. Analysis of the transient intensities of the (0,0,55) and (0,0,56) diffraction peaks, which depend on the two coordinates in a different way, allows the momentary elongations along both coordinates to be extracted. As has been discussed in Korff Schmising *et al.* (2007*a*), this procedure rests on the assumption of a constant SL period d_{SL}, a condition fulfilled within the first 4 ps after excitation. In Fig. 3(*c*) we present the time-dependent elongations along the two coordinates. The initial elongation along ξ is somewhat delayed with respect to η, a behavior caused by the finite time interval to move ξ from its initial value along the vibrational potential towards its minimum. The large change in ξ corresponds to a decrease of the ferroelectric polarization $P/P_0 = \xi/\xi_0$ by about 50%. Driving the SL motion with an even higher pump fluence we were able to completely switch off the electric polarization (Korff Schmising *et al.*, 2007*a*). Such ultrafast modulation of electric properties by launching a mechanical excitation on a nanometre scale may prove interesting for future sensor and device concepts.

From the viewpoint of basic physics, the results discussed so far demonstrate how to gain highly specific and quantitative insight into lattice motions along several anharmonically coupled vibrational coordinates. A major advantage of studying superlattices compared with bulk materials is the potential to vary and/or tailor the photogenerated stress profile by changing the optical excitation conditions. For superlattices with a limited number of layer pairs, *i.e.* sufficient optical penetration depth, all pairs can be excited. Spatially periodic excitation of, *e.g.*, a single type of SL layer generates SL lattice phonons with a specific **k** vector in the SL mini Brillouin zone. The influence of strain propagation and thermal expansion on the transient X-ray diffraction patterns is limited during the first couple of picoseconds after excitation, facilitating an analysis substantially. Finally, the different mechanisms contributing to the initial photogenerated stress can be analyzed in detail, as has been demonstrated in experiments with semiconductor (Bargheer *et al.*, 2004) and ferromagnetic (Korff Schmising *et al.*, 2008) superlattices.

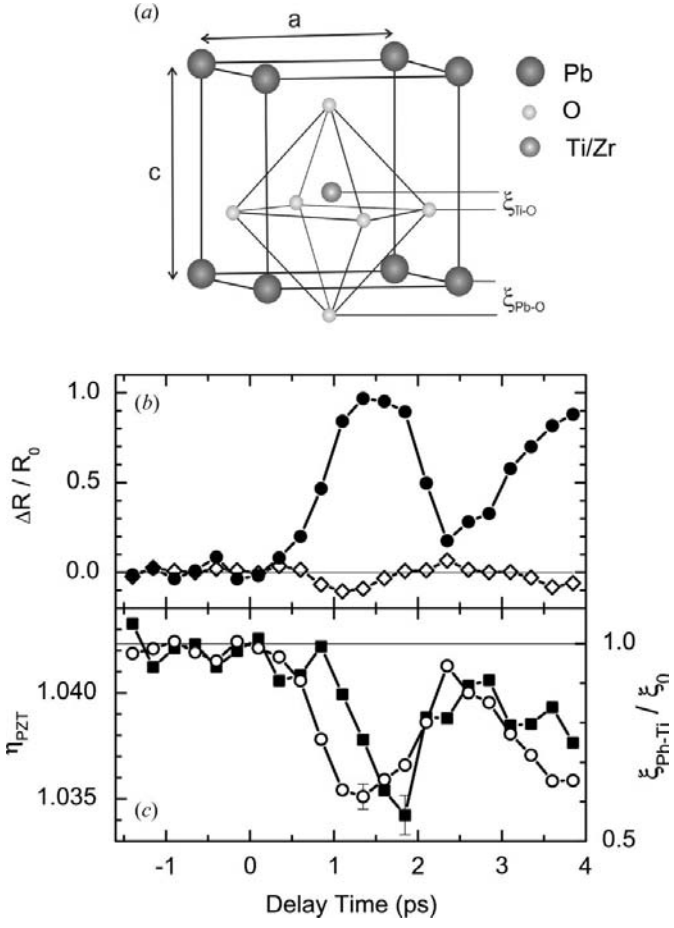

Figure 3
(*a*) Unit cell of the perovskite $PbZr_xTi_{1-x}O_3$ (PZT) with the relevant coordinates, the tetragonal distortion $\eta = c/a$ and the ferroelectric ion displacements ξ_{Pb-O} and ξ_{Ti-O}. (*b*) Transient intensity changes of the (0,0,56) (circles) and (0,0,55) (diamonds) superlattice Bragg peaks of a PZT/SRO superlattice. The normalized change of X-ray reflectivity $\Delta R/R_0 = (R - R_0)/R_0$ is plotted *versus* the pump–probe delay for a pump fluence of 5 mJ cm^{-2}. (*c*) Transient change of the tetragonality η_{PZT} (circles) and normalized soft-mode elongation ξ/ξ_0 (squares) as derived from the data in Fig. 3(*b*).

4. Ultrafast charge and lattice rearrangements in molecular crystals

Photoinduced electron and proton transfer represent basic chemical processes occurring in a large variety of (macro)-molecular systems. In the condensed phase, the reaction pathways and dynamics are determined by both the molecular potential energy surfaces and the response of the environment to the change in charge distribution and/or molecular geometry. Ultrafast optical spectroscopies have provided substantial insight into the dynamics and mechanisms of such processes (for an overview of recent research see Corkum *et al.*, 2007). In most cases, however, transient charge distributions and molecular geometries generated on a femtosecond timescale have remained uncharacterized.

Ultrafast X-ray diffraction allows for mapping transient molecular structure and for deriving time-dependent charge-density maps from the diffraction data (Collet *et al.*, 2008). Here, both Bragg diffraction from molecular single crystals and Debye–Scherrer diffraction from polycrystalline powder samples are of interest. In optical pump and X-ray probe experiments, the high density of molecular chromophores in both types of samples limits photoexcitation by femtosecond pulses to a small fraction of molecules of up to $\sim 1\%$. The penetration depth of the pump light into the sample and thus the interaction length over which the pump probe signals are integrated depend on the strength of the electronic transition excited. For one-photon excitation, the penetration depths are between 0.1 and approximately 50 µm, while two-photon excitation allows for extending the interaction length beyond 100 µm. In powder samples, elastic scattering of the pump light from the crystallites is another mechanism limiting the interaction length.

In the following we discuss two prototype diffraction studies of molecular crystals on ultrafast timescales. The first experiment with single crystals made from the charge-transfer chromophore 4-(diisopropylamino)benzonitrile (DIABN) reveals the structural response of the crystalline environment to a local photoinduced change of an electronic molecular dipole (Braun *et al.*, 2007). The second study introduces femtosecond powder diffraction to map concerted charge- and proton-transfer processes in ammonium sulfate [$(NH_4)_2SO_4$] and provides transient charge-density maps for this system.

4.1. Structural dynamics of dipole solvation

DIABN (Fig. 4*a*) crystallizes in a monoclinic structure [*C*12/*c*1 (No. 15)] with 16 molecules in a unit cell (Frey *et al.*, 2004). There are four molecular layers perpendicular to the *c* axis per unit cell, each containing pairs of molecules of parallel or anti-parallel orientation. Optical excitation of the DIABN chromophore at wavelengths around 400 nm populates the locally excited (LE) state of DIABN from which an intramolecular charge-transfer (CT) state is formed. This process is connected with a change in the molecular dipole moment from 8.5 Debye in the electronic ground state to approximately 17 Debye in the CT state (Grabowski *et al.*, 2003). The formation time of the CT state has been studied both by time-resolved fluorescence and transient vibrational absorption measurements and a rise time of 11 ps has been derived (Techert & Zachariasse, 2004; Root, 2006).

In the femtosecond diffraction experiment, a 400 nm pump pulse (fluence 0.15 mJ cm^{-2}) excites approximately 10^{-4} of the DIABN chromophores in a 50 µm thick single crystal. The optical transmission of the crystal is 0.5, allowing for a spatially homogeneous excitation of molecules. The resulting structural change of the environment consisting of mainly unexcited DIABN molecules is probed by diffracting/transmitting femtosecond hard X-ray pulses of 0.154 nm wavelength and 200 fs duration. A multilayer X-ray mirror serves to focus the X-ray beam onto the sample. We measure the reflected X-ray intensity integrated over the (004) and (006) Bragg peaks [steady-state reflectivities $R(004) \simeq 0.003$ and $R(006) \simeq 0.001$] and the transient X-ray transmission.

Time-resolved diffraction data are presented in Figs. 4(*b*) and (*c*). Strong changes of X-ray transmission and reflectivity are found on the (004) and (006) Bragg diffraction peaks,

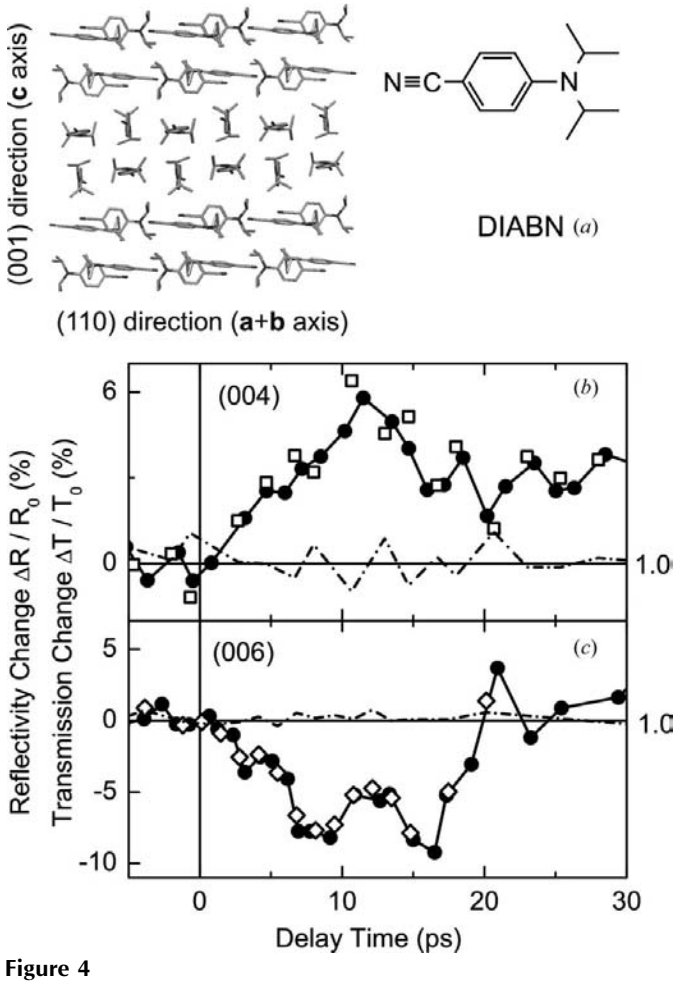

Figure 4
(*a*) Crystal structure and molecular structure of DIABN. (*b*), (*c*) Time-resolved change of X-ray transmission (open symbols) and reflection (solid symbols) measured for the (004) and (006) Bragg angles (solid lines are a guide to the eye). Dash–dotted lines: Ratio of the X-ray reflectivity and transmission change for the respective Bragg angle of the crystal as a function of delay time. The constant ratio of 1 shows that amplitude and time evolution of transmission and reflectivity changes are identical.

which are of the order of $\Delta T/T_0 = (T(t) - T_0)/T_0 \simeq 0.1$ [$T(t)$, T_0: transmission with and without excitation]. The transients show a rise with a time constant of approximately 10 ps, followed by oscillatory contributions at longer delay times that reflect lattice dynamics. In parallel to the transmission changes, reflectivity changes with the same sign and amplitude are observed, *i.e.* $\Delta R/R_0 = \Delta T/T_0$ for both Bragg angles. The angular positions of the Bragg peaks and thus the size of the elementary cells of the crystal remain unchanged within the range of time delays shown in Figs. 4(*b*) and (*c*).

The transient changes of X-ray transmission and reflectivity display a rise time determined by the 11 ps buildup time of the CT state. This fact shows that the change of crystal structure is driven by the change of molecular dipole moment in the small fraction of excited DIABN molecules. The large amplitude of the transient X-ray signals $\Delta R/R_0$ and $\Delta T/T_0$ of up to 10% demonstrates that a major fraction of unexcited DIABN molecules around the very few excited chromophores must be involved in the structure changes. A local geometry change of the 10^{-4} excited chromophores cannot account for such strong signals. We conclude that the observed structure changes are due to the response of the unexcited crystalline environment to the local change of the photoexcited dipole. The very similar buildup times of the CT state in the excited chromophores and of the X-ray signals shows that the environment responds with negligible delay to the dipole change.

The experimental result $\Delta T/T_0 = \Delta R/R_0$ (for delay times ≤ 100 ps) demonstrates that diffuse X-ray scattering (Welberry & Butler, 1995) predominates and both the transient reflectivity $R(t) = R_N\{1 - \exp[-2\mu(t)L]\}/2\mu(t)$ (R_N: reflectivity per unit crystal thickness; L: crystal length) and transmission $T(t) = \exp[-\mu(t)L]$ are governed by the transient X-ray extinction coefficient $\mu(t)$ of the crystal. Steady-state X-ray transmission measurements also show that diffuse scattering represents the dominant contribution to $\mu(t)$. Braun *et al.* (2007) describe a theoretical calculation of the anisotropic extinction coefficient of the DIABN crystal geometry for the Cu $K\alpha$ wavelength of λ = 0.154 nm. This calculation suggests that at least all 110 electrons of an individual DIABN chromophore contribute coherently to the X-ray extinction. In Fig. 5(*a*) the anisotropic extinction coefficient calculated for an ensemble of 100 DIABN molecules in the crystal geometry of Fig. 4(*a*) is shown as a contour plot. The solid line in Fig. 5(*a*) represents a cut through the anisotropic distribution for ϕ_0 = 150° around small values of $\Theta_{Bragg} = 90 - \Theta_0$°. The pronounced anisotropy of the extinction coefficient along the orientation of the molecules is mainly determined by the spatial positions of the core electrons of carbon and nitrogen. In the lattice planes of the crystal shown in Fig. 4(*a*), the molecules are aligned along these directions and thus give rise to strong anisotropic diffuse X-ray scattering.

The change in the dipole moment of the (highly diluted) photoexcited DIABN chromophores results in a change of their electric field $\mathbf{E}_{loc}$, exerting a torque of $\mathbf{M} = \mathbf{d}_0 \times \mathbf{E}_{loc}$ on the (ground state) dipoles of the surrounding unexcited molecules. The long-range dipole field of the chromophore is of cylindrical symmetry and thus induces small rotations of molecules in the crystal lattice, as shown schematically in Fig. 5(*b*). Such a reorientation lowers the energy of the CT state by reducing the dipole–dipole interaction energies, *i.e.* the excited dipole is being 'solvated' (van der Zwan & Hynes, 1985). The reorientation of unexcited dipoles changes the ensemble-averaged anisotropic X-ray extinction coefficient towards a spherical symmetry, the latter being characterized by a scattering cross section per electron that is independent of Θ_{Bragg} (dash–dotted line in Fig. 5*a*). As a result of the transiently decreased cross section on the (004) Bragg peak (*cf.* short vertical arrows in Fig. 5*a*), the measured (004) reflection and transmission increase (Fig. 4*b*). On the (006) Bragg peak, the transient cross section is enhanced and thus one observes a reflection and transmission decrease (Fig. 4*c*). The degree of angular reorientation depends on the local electric field acting on the respective ground state dipole, *i.e.*

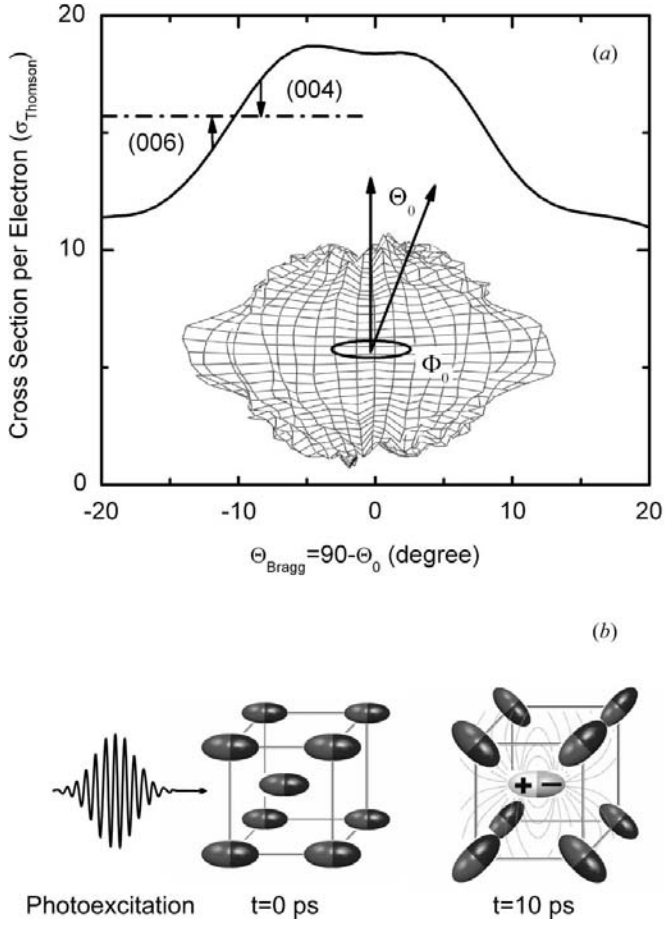

Figure 5
(*a*) Calculated elastic X-ray scattering cross section per electron for a crystal consisting of 100 DIABN molecules as a function of the Bragg angle (X-ray wavelength Cu $K\alpha$ 0.154 nm). Inset: Contour plot with polar diagram of the anisotropic scattering cross section along the axis of the molecules aligned in the crystal structure. The polar coordinate system is aligned with the crystal axes *a*, *b* and *c*. (*b*) Schematic of structural changes connected with polar solvation. The ultrashort excitation pulse initiates an intramolecular charge transfer which results in a dipole change building up on a 10 ps timescale. The surrounding polar molecules reorient in the electric field of the dipole owing to the torque exerted on them.

on the distance from the excited chromophore. For the relevant electric fields between 10^6 and 10^{10} V m^{-1}, and the elastic molecular torque constant of $D_{\rm rot} \simeq 10000$ cm^{-1}, molecular rotation angles can be estimated as being from 0.01° up to 10°. The absence of changes in the angular positions of the Bragg peaks demonstrates that translational motions changing the separation of lattice planes play a negligible role. Our results are the first identifying the structural dynamics connected with a molecular dipole solvation process directly.

4.2. Transient charge-density maps of ammonium sulfate

X-ray diffraction is a key method for determining charge-density maps of condensed matter on an atomic length scale (Coppens, 1997). While studies of equilibrium time-averaged electron distributions have reached a high level of sophistication, information on transient changes of such distributions are limited, in particular when it comes to the ultrafast timescales of atomic motions and elementary chemical processes. In the following we describe the first femtosecond powder diffraction experiments which provide direct access to transient charge-density maps. As a model system, the ionic hydrogen-bonded material ammonium sulfate [AS, $(NH_4)_2SO_4$] was studied.

At T = 300 K AS crystallizes in an orthorhombic structure belonging to the space group *Pnam*, with four $(NH_4)_2SO_4$ entities per unit cell (Fig. 6*a*; Schlemper & Hamilton, 1966; Ahmed *et al.*, 1987). The dimensions of the unit cell are a = 7.78, b =10.64 and c = 5.99 Å and the material is paraelectric. At a temperature of T = 223 K, AS undergoes a structural phase transition into a ferroelectric phase of lower symmetry and the space group $Pna2_1$. Here we are studying non-equilibrium structural changes initiated by femtosecond photoexcitation of AS at T = 300 K. A powder sample is excited *via* three-photon absorption of 50 fs pump pulses at 400 nm and structure changes are mapped by diffracting ultrashort Cu $K\alpha$ pulses from the excited sample. The angular position and the intensity of approximately 20 Debye–Scherrer diffraction rings are measured simultaneously as a function of the pump–probe delay. The ring patterns are recorded with a large-area X-ray CCD detector.

In Fig. 7(*a*) we present the diffraction pattern of the unexcited AS powder as measured with our femtosecond plasma source (solid line). The intensity integrated over each diffraction ring is plotted as a function of diffraction angle. After photoexcitation of the sample, the intensity of the rings undergoes pronounced changes as shown in Fig. 7(*b*) for a pump–probe delay of 65 fs. In Fig. 8 the time evolution of the intensity changes is plotted for three selected rings on a short timescale from −0.5 to 0.5 ps, and on a longer picosecond timescale. The transients exhibit pronounced oscillations with the 650 fs period of the 50 cm^{-1} A_g phonon of AS.

The change in the (111) intensity (bottom panel) displays a very fast rise within the first 100 fs, demonstrating the very high time resolution of the experiment. The dashed line represents a fit through the data points, giving the time-integrated cross-correlation function of the pump and probe pulses. The time derivative of this curve (upper part) is proportional to the cross-correlation function of 130 fs width. This result points to a duration of the X-ray probe pulses of $\leq$100 fs. It is important to note that the angular positions of all the diffraction rings remain unchanged over the time range of Fig. 8. Thus, changes in the average positions of the heavier atoms S, N and O in the unit cell are minor and the unit-cell volume remains unchanged.

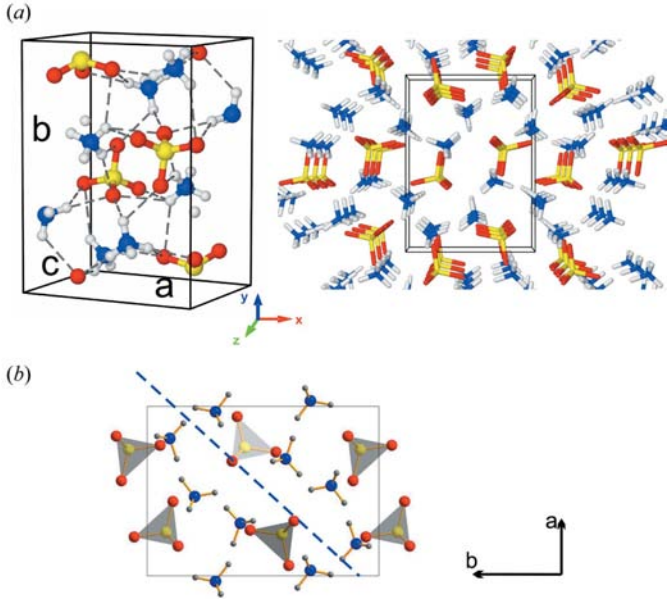

Figure 6
(*a*) Unit cell of ammonium sulfate (left) with sulfate SO_4^{2-} and ammonium NH_4^+ groups (yellow: S atoms, red: O, blue: N, gray: H, dashed lines: hydrogen bonds). View of the lattice (right) into the z direction. (*b*) Lattice plane defined by the z direction and the line linking the O atoms 1 and 2 of opposite sulfate groups (dashed line).

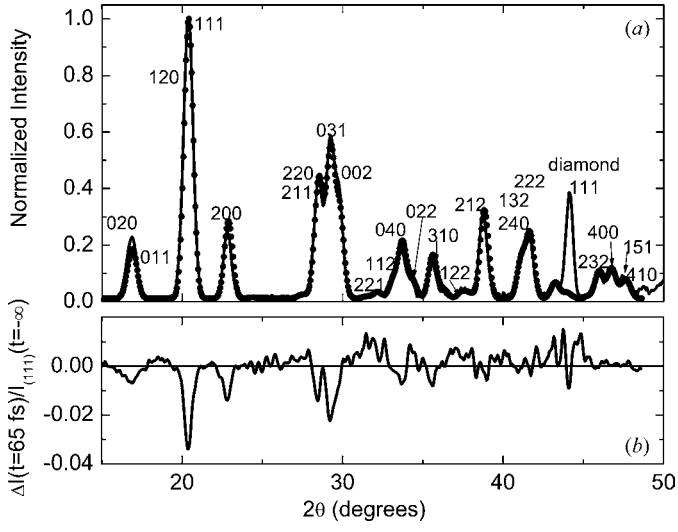

Figure 7
(*a*) Measured (solid line) and calculated (dots) intensity profile of the Debye Scherrer ring pattern of AS as a function of 2θ (θ: diffraction angle). The intensities are normalized to that of the (111) peak. (*b*) Intensity change of the rings observed 65 fs after excitation of the sample.

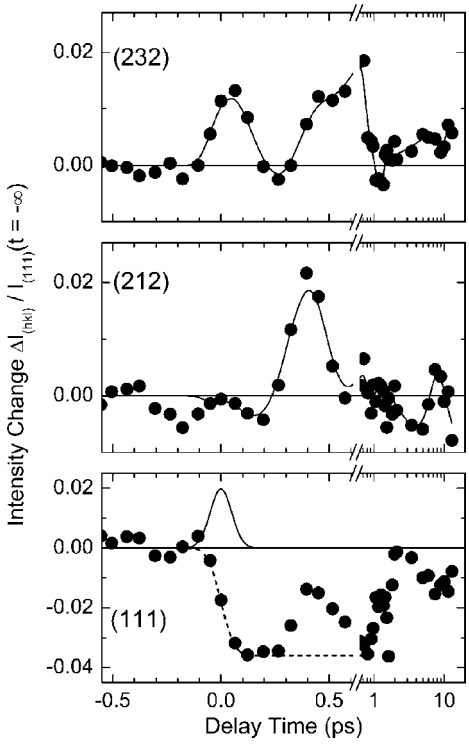

Figure 8
(*a*) Changes in intensity (solid circles) of particular Debye–Scherrer rings as a function of time delay between the optical pump and X-ray probe. The thin solid lines are guides to the eye. The dashed line in the bottom panel represents a fit to the data giving the time-integrated cross-correlation function of optical pump and X-ray probe pulses. The time derivative of this fit plotted in the upper part is the cross-correlation function.

The intensity of the Debye–Scherrer diffraction rings is determined by the respective structure factor F_{hkl} of the AS unit cell (Warren, 1969). F_{hkl} contains the atomic form factors given by the Fourier transforms of the spatial electron density $\rho_e(x, y, z)$ with the respective reciprocal-lattice vector G_{hkl}. We first analyzed the steady-state diffraction pattern (Fig. 7*a*) by calculating the structure factors with the atomic positions in AS determined in neutron diffraction studies and the atomic form factors. The result (dots in Fig. 7*a*) is in excellent agreement with our measurements.

The changes of diffracted intensity upon photoexcitation are due to the modified transient $\rho_e(x, y, z)$ which is extracted from the time-resolved data in the following way:

The time-dependent intensity diffracted from a photo-excited crystallite is given by

$$I_{hkl}(t, \eta) = C_{hkl}\left|\eta\,|F^{ex}_{hkl}(t)|\exp(i\phi_{hkl}) + [1-\eta\,]|F^{gr}_{hkl}|\exp(i\phi_{hkl})\right|^2. \quad (1)$$

Here, C_{hkl} contains all the reflection-dependent factors for powder diffraction except for the transient $[F^{ex}_{hkl}(t)]$ and steady-state (F^{gr}_{hkl}) structure factors. C_{hkl} is calibrated with the help of the steady-state diffraction pattern. The phase of the structure factor is set taking into account the symmetry of the AS structure. At T = 300 K, the initial orthorhombic AS structure displays inversion symmetry and thus the phase is $\phi_{hkl} = 0$ or π. Our time-resolved diffraction data from the photoexcited AS structure demonstrate negligible changes in the positions of the heavier atoms which predominantly

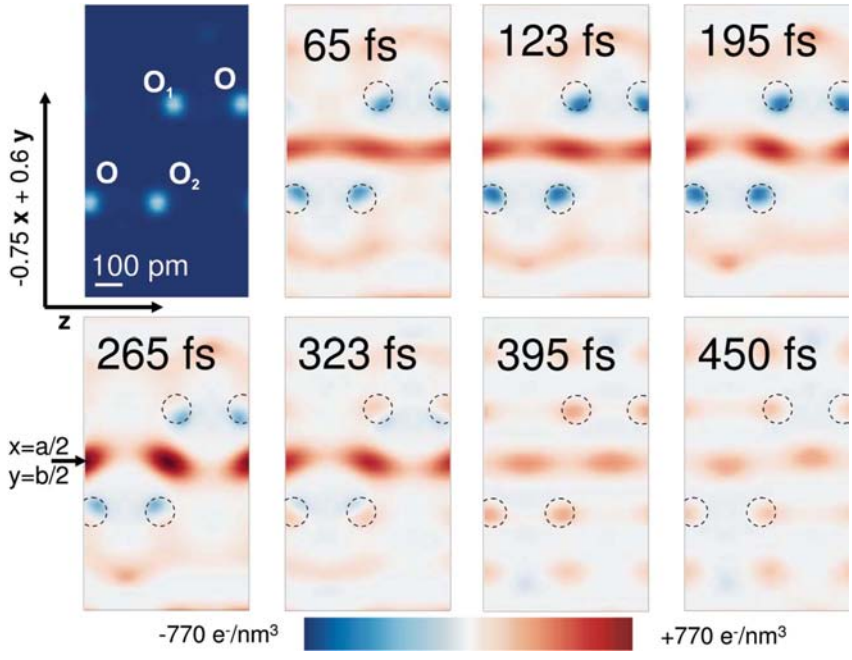

Figure 9
Charge-density maps derived from the diffraction data for a plane containing the z axis and the line linking the O atoms 1 and 2 of opposite sulfate groups (*cf.* Fig. 6*b*). The upper-left panel shows the equilibrium charge density $\rho(x, y, z)$, the other panels show the change in charge density $\Delta\rho(x, y, z)$ for different time delays after photoexcitation.

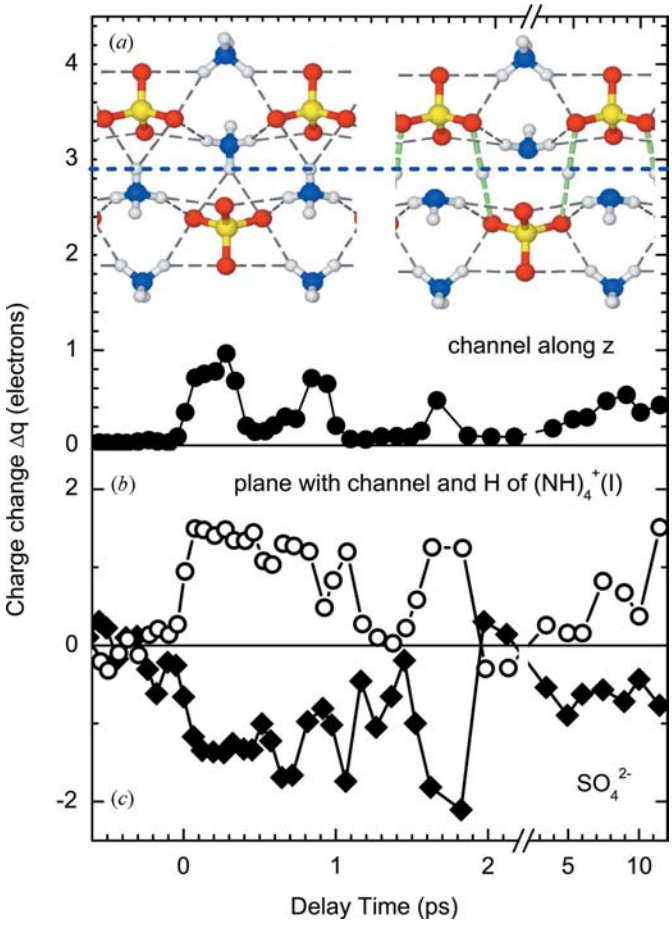

Figure 10
(*a*) Total charge change in the channel region as a function of pump–probe delay. The charge change is plotted in units of elementary charge. (*b*) Transient change of electronic charge integrated in the plane containing the charge channel and the proton positions on the $(NH_4)^+$(I) groups. (*c*) Same for the two SO_4^{2-} groups close to the electron channel. The transients in (*b*) and (*c*) display the same time evolution with opposite signs of the charge changes.

determine the diffraction pattern. Thus, inversion symmetry is essentially preserved after photoexcitation and the phase of the structure factor remains unchanged. The quantity $\eta \simeq 0.06 \ll 1$ is the fraction of photoexcited, structurally modified unit cells of the crystallite. For small η the following linear relation between the change of the structure factor and the measured intensity change can be derived:

$$\eta \Delta F_{hkl}(t) = \eta\big(|F^{\rm ex}_{hkl}(t)| - |F^{\rm gr}_{hkl}|\big) \simeq \frac{\Delta I^{\rm exp}_{hkl}(t)}{2C_{hkl}|F^{\rm gr}_{hkl}|}, \qquad (2)$$

with $\Delta I^{\rm exp}_{hkl}(t) = [I_{hkl}(t, \eta) - I^0_{hkl}]$ and I^0_{hkl} the intensity diffracted before excitation of the sample. The change of structure factor gives the change of spatial electron density by

$$\Delta\rho_{\rm e}(x, y, z, t) = \sum_{hkl} \frac{\Delta F_{hkl}(t)\exp(i\phi_{hkl})}{abc} \times \cos\left(\frac{2\pi hx}{a} + \frac{2\pi ky}{b} + \frac{2\pi lz}{c}\right). \qquad (3)$$

Equations (1)–(3) allow for deriving transient charge-density maps from the measured quantities $\Delta I^{\rm exp}_{hkl}(t)$ and the atomic positions.

In Fig. 9 we present charge-density maps for a plane containing the z axis and the line connecting the O atoms 1 and 2 of opposite SO_4^{2-} groups (*cf.* Fig. 6*b*). The figure combines the equilibrium charge density (upper left) and its change $\Delta\rho(x, y, z)$ for seven different time delays after excitation. The most striking photoinduced change consists of the formation of a channel-like geometry of enhanced electron density along the z axis. Such a feature occurs at the spatial position $(x, y, z) = (0, 0, z)$ and $(0.5a, 0.5b, z)$ in the unit cell with local maxima of electron density at $(0, 0, 0)$, $(0, 0, 0.5c)$, $(0.5a, 0.5b, 0)$ and $(0.5a, 0.5b, 0.5c)$. In the AS equilibrium structure (Fig. 6) there are no lattice atoms at those positions. The channel region displays a pronounced lateral confinement with a diameter in the xy plane of approximately $2a_{\rm B}$, with $a_{\rm B}$ being the Bohr radius of the H atom. This finding points to a stabilization of the channel geometry by (positively charged) protons which move from the neighboring $(NH_4)^+$ groups into positions between the O atoms 1 and 2 of adjacent SO_4^{2-} groups (inset of Fig. 10*a*). The formation of this hydrogen-bonded new geometry requires a concerted charge and proton transfer. This process occurs within the first 100 fs after photoexcitation, as is evident from the charge-density map for 65 fs displaying the channel geometry.

The electron density in the channel shows periodic oscillations with a frequency of 50 cm^{-1} of the A_g phonon (Fig. 10*a*). This lattice mode modulates the O_1-O_2 distance periodically and induces a periodic charge and proton transfer between the channel and the original site of the proton on the $(NH_4)^+$ group. The overall charge in the plane defined by the channel and the line connecting the proton sites on two neighboring $(NH_4)^+$ groups is constant during the oscillation (Fig. 10*b*). Concomitantly, the charge on the two $(SO_4)^{2-}$ groups close to the channel remains depleted (Fig. 10*c*), demonstrating again that the S atoms represent the main supply of charge for the channel formation. The results shown in Figs. 9 and 10 underline the potential of femtosecond X-ray powder diffraction to unravel elementary changes of molecular structure in real time and characterize the transient charge distributions in a quantitative way.

5. Conclusions

The results discussed in this article show that femtosecond X-ray diffraction using laser-driven plasma sources provides quantitative insight into ultrafast structural changes and into the driving mechanisms behind them. With both single-crystal Bragg and powder Debye–Scherrer methods for real-time mapping of structural dynamics, a very wide range of materials becomes accessible. Apart from photoexcitation *via* electronic transitions, femtosecond vibrational excitation is readily implemented for driving nuclear motions directly. Powder diffraction patterns consisting of a large number of diffraction rings allow for deriving transient charge-density maps, a new research area that is particularly relevant for studies of

materials with correlated electron and spin systems and for a broad range of biomolecular systems. Future work will both focus on the development of even better laser-driven sources and address structural dynamics in new classes of materials.

We would like to acknowledge the important contributions of our present and former co-workers C. von Korff Schmising, N. Zhavoronkov, M. Bargheer, Y. Gritsai, M. Kiel, A. Harpoeth, Z. Ansari and M. Zamponi to the results reported here. We thank M. Braun, W. Zinth, University of Munich, and their co-workers as well as D. Hesse, I. Vrejoiu and M. Alexe, MPI for the Physics of Microstructures, Halle, for fruitful collaborations. This work has been supported in part by the Deutsche Forschungsgemeinschaft through the Schwerpunktprogramm 1134.

References

Ahmed, S., Shamah, A. M., Kamel, R. & Badr, Y. (1987). *Phys. Status Solidi. A*, **99**, 131–140.

Als-Nielsen, J. & McMorrow, D. (2001). *Elements of Modern X-Ray Physics*. New York: Wiley.

Bargheer, M., Zhavoronkov, N., Bruch, R., Legall, H., Stiel, H., Woerner, M. & Elsaesser, T. (2005). *Appl. Phys. B*, **80**, 715–719.

Bargheer, M., Zhavoronkov, N., Gritsai, Y., Woo, J. C., Kim, D. S., Woerner, M. & Elsaesser, T. (2004). *Science*, **306**, 1771–1773.

Bargheer, M., Zhavoronkov, N., Woerner, M. & Elsaesser, T. (2006). *ChemPhysChem*, **7**, 783–792.

Beaud, P., Johnson, S. L., Streun, A., Abela, R., Abramsohn, D., Grolimund, D., Krasniqi, F., Schmidt, T. Schlott, V. & Ingold, G. (2007). *Phys. Rev. Lett.* **99**, 174801.

Braun, M., Korff-Schmising, C. von, Kiel, M., Zhavoronkov, N., Dreyer, J., Bargheer, M., Elsaesser, T., Root, C., Schrader, T. E., Gilch, P., Zinth, W. & Woerner, M. (2007). *Phys. Rev. Lett.* **98**, 248301.

Cavalleri, A., Wall, S., Simpson, C., Statz, E., Ward, D. W., Nelson, K. A., Rini, M. & Schoenlein, R. W. (2006). *Nature (London)*, **442**, 664–666.

Collet, E., Cointe, M. B. L., Lorenc, M. & Cailleau, H. (2008). *Z. Kristallogr.* **223**, 272–282.

Colvard, C., Gant, T. A., Klein, M. V., Merlin, R., Fischer, R., Morkoc, H. & Gossard, A. C. (1985). *Phys. Rev. B*, **31**, 2080–2091.

Coppens, P. (1997). *X-ray Charge Densities and Chemical Bonding*. New York: Oxford University Press.

Corkum, P., Jonas, D., Miller, R. J. D. & Weiner, A. M. (2007). Editors. *Ultrafast Phenomena XV*. Berlin: Springer.

Esaki, L. & Tsu, R. (1970). *IBM J. Dev.* **14**, 61–65.

Frey, W., Root, C., Gilch, P. & Braun, M. (2004). *Z. Kristallogr. New Cryst. Struct.* **219**, 291–292.

Grabowski, Z. R., Rotkiewicz, K. & Rettig, W. (2003). *Chem. Rev.* **103**, 3899–4032.

Jiang, Y., Lee, T., Li, W., Ketwaroo, G. & Rose-Petruck, C. G. (2002). *Opt. Lett.* **27**, 963–965.

Khan, S., Holldack, K., Kachel, T., Mitzner, R. & Quast, T. (2006). *Phys. Rev. Lett.* **97**, 074801.

Kmetec, J. D., Gordon III, C. L., Macklin, J. J., Lemoff, B. E., Brown, G. S. & Harris, S. E. (1991). *Phys. Rev. Lett.* **68**, 1527–1530.

Korff Schmising, C. von, Bargheer, M., Kiel, M., Zhavoronkov, N., Woerner, M., Elsaesser, T., Vrejoiu, I., Hesse, D. & Alexe, M. (2006). *Phys. Rev. B*, **73**, 212202.

Korff Schmising, C. von, Bargheer, M., Kiel, M., Zhavoronkov, N., Woerner, M., Elsaesser, T., Vrejoiu, I., Hesse, D. & Alexe, M. (2007*a*). *Phys. Rev. Lett.* **98**, 257601.

Korff Schmising, C. von, Bargheer, M., Kiel, M., Zhavoronkov, N., Woerner, M., Elsaesser, T., Vrejoiu, I., Hesse, D. & Alexe, M. (2007*b*). *Appl. Phys. B*, **88**, 1–4.

Korff Schmising, C. von, Harpoeth, A., Zhavoronkov, N., Ansari, Z., Aku-Leh, C., Woerner, M., Elsaesser, T., Bargheer, M., Schmidbauer, M., Vrejoiu, I., Hesse, D. & Alexe, M. (2008). *Phys. Rev. B*, **78**, 060404(R).

Korn, G., Thoss, A., Stiel, H., Vogt, U., Richardson, M., Elsaesser, T. & Faubel, M. (2002). *Opt. Lett.* **27**, 866–868.

Krost, A., Bauer, G. & Woitok, J. (1996). *Optical Characterization of Epitaxial Semiconductor Layers*, edited by G. Bauer & W. Richter, pp. 287–391. Berlin: Springer.

Lichtensteiger, C., Triscone, J. M., Junquera, J. & Ghosez, P. (2005). *Phys. Rev. Lett.* **94**, 047603.

Lindenberg, A. M. *et al.* (2005). *Science*, **308**, 392–395.

Rischel, C., Rousse, A., Uschmann, I., Albouy, P. A., Geindre, J. P., Audebert, P., Gauthier, J. C., Förster, E., Martin, J. L. & Antonetti, A. (1997). *Nature (London)*, **390**, 490–492.

Root, C. (2006). PhD thesis, University of Munich, Germany.

Rousse, A., Rischel, C., Fourmaux, S., Uschmann, I., Sebban, S., Grillon, G., Balcou, P., Förster, E., Geindre, J. P., Audebert, P., Gauthier, J. C. & Hulin, D. (2001). *Nature (London)*, **410**, 65–68.

Rousse, A., Rischel, C. & Gauthier, J. C. (2001). *Rev. Mod. Phys.* **73**, 17–31.

Sanjurjo, J. A., Lopez-Cruz, E. & Burns, G. (1983). *Solid State Commun.* **48**, 221–224.

Schlemper, E. O. & Hamilton, W. C. (1966). *J. Chem. Phys.* **44**, 4498–4509.

Schoenlein, R. W., Chattopadhyay, S., Chong, H. H. W., Glover, T. E., Heimann, P. A., Shank, C. V., Zholents, A. A. & Zolotorev, M. S. (2000). *Science*, **287**, 2237–2239.

Service, R. F. (2002). *Science*, **298**, 1356–1358.

Siders, C. W., Cavalleri, A., Sokolowski-Tinten, K., Toth, C., Guo, T., Kammler, M., von Hoegen, M. H., Wilson, K. R., von der Linde, D. & Barty, C. P. J. (1999). *Science*, **286**, 1340–1342.

Sokolowski-Tinten, K., Blome, C., Blums, J., Cavalleri, A., Dietrich, C., Tarasevitch, A., Uschmann, I., Förster, E., Kammler, M., Horn-von-Hoegen, M. & von der Linde, D. (2003). *Nature (London)*, **422**, 287–289.

Techert, S. & Zachariasse, K. A. (2004). *J. Am. Chem. Soc.* **126**, 5593–5600.

Warren, B. E. (1969). *X-Ray Diffraction.* New York: Dover.

Welberry, T. R. & Butler, B. D. (1995). *Chem. Rev.* **95**, 2369–2403.

Wolfram, T. & Ellialtioglu, S. (2006). *Electronic and Optical Properties of d-Band Perovskites.* Cambridge University Press.

Zamponi, F., Ansari, Z., von Korff Schmising, C., Rothhardt, P., Zhavoronkov, N., Woerner, M., Elsaesser, T., Bargheer, M., Trobitzsch-Ryll, T. & Haschke, M. (2009). *Appl. Phys. A*, **96**, 51–58.

Zhavoronkov, N., Gritsai, Y., Bargheer, M., Woerner, M., Elsaesser, T., Zamponi, F., Uschmann, I. & Förster, E. (2005). *Opt. Lett.* **30**, 1737–1739.

Zwan, G. van der & Hynes, J. T. (1985). *J. Phys. Chem.* **89**, 4181–4188.